Magnetic Resonance Letters 7 (2027) 200292

Contents lists available at ScienceDirect

Magnetic Resonance Letters

journal homepage: www.keaipublishing.com/MRL

Research Article

Predictions and cross-center validation of IDH status and 1p/19q status in adult diffuse glioma with non-invasive magnetic resonance spectroscopy

Zhangren Tu [a,b,j,1], Wanjun Hu [c,1], Jialve Zhang [d,j,1], Zhen Xing [e,f], Jiamin Li [e,f], Jingjing Xu [a,b], Meijin Lin [b,g], Xianwang Jiang [b,h], Dairong Cao [e,f,*], Jing Zhang [c,**], Di Guo [i,***], Xiaobo Qu [j]

[a] Department of Electronic Science, Xiamen University, Xiamen, 361102, China
[b] Xiamen University-Neusoft Medical Magnetic Resonance Imaging Joint Research and Development Center, Fujian Provincial Key Laboratory of Plasma and Magnetic Resonance, Xiamen, 361102, China
[c] Department of Nuclear Magnetic Resonance, Gansu Province Clinical Research Center for Functional and Molecular Imaging, The Second Hospital & Clinical Medical School, Lanzhou University, Lanzhou, 730030, China
[d] Pen-Tung Sah Institute of Micro-Nano Science and Technology, Xiamen University, Xiamen, 361102, China
[e] Department of Radiology, The First Affiliated Hospital, Fujian Medical University, Fuzhou, 350005, China
[f] Department of Radiology, National Regional Medical Center, Binhai Campus of the First Affiliated Hospital, Fujian Medical University, Fuzhou, 350212, Fujian, China
[g] College of Ocean & Earth Sciences, Xiamen University, Xiamen, 361102, China
[h] Shanghai Neusoft Medical Technology Co. Ltd, Shanghai, 200241, China
[i] School of Computer and Information Engineering, Fujian Engineering Research Center for Medical Data Mining and Application, Xiamen University of Technology, Xiamen, 361024, China
[j] Shenzhen Research Institute of Xiamen University, Shenzhen, 518000, China

ARTICLE INFO

Article history:
Received 2 February 2026
Received in revised form 15 May 2026
Accepted 18 May 2026
Available online 1 June 2026

Keywords:
Adult diffuse glioma
Molecular subtyping
Magnetic resonance spectroscopy
Isocitrate dehydrogenase (IDH)

ABSTRACT

This study developed and validated a non-invasive multi-metabolite magnetic resonance spectroscopy framework for preoperative molecular subtyping of adult diffuse gliomas. Using a cross-center, cross-vendor cohort of 268 patients, 48 features derived from 18 metabolites were systematically evaluated to identify discriminative metabolic signatures for predicting IDH mutation and 1p/19q codeletion status. The integrated metabolic model showed robust intra-center and cross-center performance for IDH prediction, with AUCs of 0.906 and 0.857, respectively, and for 1p/19q prediction, with AUCs of 0.858 and 0.787, respectively. These results suggest that synergistic metabolic profiling support molecular assessment in patients who may not be suitable for invasive biopsy.

* Corresponding author. Department of Radiology, The First Affiliated Hospital, Fujian Medical University, Fuzhou, 350005, China.
** Corresponding author.
*** Corresponding author.
E-mail addresses: dairongcao@fjmu.edu.cn (D. Cao), ery_zhangjing@lzu.edu.cn (J. Zhang), guodi@xmut.edu.cn (D. Guo).
Peer review under the responsibility of Innovation Academy for Precision Measurement Science and Technology (APM), CAS.
[1] Equal contribution.

https://doi.org/10.1016/j.mrl.2026.200292

1. Introduction

Adult-type diffuse gliomas are the most common malignant primary central nervous system tumors [1]. The 5th edition of the WHO classification of central nervous system tumors (WHO 2021) places increasing emphasis on molecular alterations, categorizing gliomas primarily by IDH mutant and 1p/19q codeletion status into three major types: glioblastoma (IDH-wildtype), astrocytoma (IDH-mutant, 1p/19q non-codeleted), and oligodendroglioma (IDH-mutant, 1p/19q codeleted) [2].

Magnetic resonance spectroscopy (MRS) is a non-invasive technique capable of profiling *in vivo* metabolite concentrations, thereby offering direct insight into tumor metabolism. These metabolic profiles hold promise as biomarkers for molecular subtyping, underpinned by the regulatory role of genetic expression in metabolic pathways. A key example is IDH: while wild-type IDH converts isocitrate to α-ketoglutarate (α-KG), mutant IDH gains neomorphic activity, reducing α-KG to the oncometabolite 2-hydroxyglutarate (2HG) [3]. Consequently, MRS-based detection of 2HG enables non-invasive identification of IDH mutations, illustrating a direct link between genetics and metabolic phenotyping.

Previous MRS studies have identified several potential metabolic biomarkers—such as 2HG, glutathione (GSH), glutamine/glutamate (Glx), alanine (Ala), myo-inositol (mI), and total choline (tCho)—for predicting IDH status, and cystathionine for 1p/19q status (Table 1).

However, these findings are largely fragmented, as each study typically focused on a limited subset of metabolites, derived from relatively small cohorts ($n < 50$ in most cases). While large-scale validation (n~1000) of 2HG as a biomarker has been achieved through invasive mass spectrometry (Table 2) [19], a comprehensive, multi-metabolite feature analysis using non-invasive MRS has been lacking.

In contrast, our study establishes the largest MRS dataset to date ($n = 268$) for non-invasive molecular subtyping, validated across multiple centers. More importantly, we move beyond the conventional single-metabolite approach by systematically evaluating 48 distinct classification features derived from 19 metabolites. This high-dimensional perspective allows us to perform an integrated multi-metabolite analysis that not only identifies synergistic effects among metabolite signatures but also provides a complete quantitative ranking of all 48 features by importance. Thereby, we offer a comprehensive and systematic view of metabolic signatures for glioma classification using a completely non-invasive MRS protocol.

2. Methods

This study collected MRS data from 370 adult patients with diffuse glioma. The dataset was derived from two clinical centers involving two scanner vendors. Specifically, the internal cohort (Siemens) comprised 308 cases acquired using Siemens Prisma and Skyra 3T scanners across two campuses of the First Affiliated Hospital of Fujian Medical University. The external cohort (Philips) included 62 cases obtained using Philips 3T scanners at the Second Hospital & Clinical Medical School of Lanzhou University. Intra-center patient data were approved by the ethics committee (No. MRCTA, ECFAH of FMU [2020] 312). Cross-center patient data were approved by the ethics committee (2024A-181) of the Second Hospital & Clinical Medical School, Lanzhou University. Molecular subtyping for all patients was determined via immunohistochemistry (IHC) and gene sequencing. Cases with insufficient pathological information were excluded. The volumes of interest for MRS were positioned to include the viable enhancing tumor core, sparing any cystic, hemorrhagic, or necrotic changes.

Detailed MRS acquisition parameters are provided in Table S1. The raw spectral data underwent preprocessing as follows: (1) Fourier transformation was applied, followed by residual water peak removal using Hankel singular value decomposition (HSVD) via a custom-developed script; (2) Frequency pre-correction was performed by referencing the creatine (Cr) peak at 3.02 ppm; (3) the FID-A toolbox [28] was utilized to calculate the full width at half maximum (FWHM) and signal-to-noise ratio (SNR), with low-quality data (FWHM > 0.15 ppm, SNR < 5) being rigorously excluded. The preprocessed data were then exported in RAW format for quantitative analysis using LCModel [29]. As illustrated in Fig. S1, all data were processed using a unified pipeline. Furthermore, to minimize spectral fitting discrepancies arising from vendor-specific and sequence parameter variations, we generated quantum-simulated basis-sets tailored to the specific hardware and acquisition parameters of each site. This approach ensures that fitting differences do not confound subsequent feature extraction. Fig. 1(a) presents representative LCModel quantification results for each subtype of adult diffuse glioma. The patient inclusion flowchart is shown in Fig. 1(b). For the intra-center cohort ($n = 308$), 29 cases were excluded due to poor data quality and 50 excluded due to incomplete clinical information, leaving 229 patients for analysis; similarly, for the cross-center cohort ($n = 62$), 17 cases were excluded due to poor data quality and 6 excluded due to incomplete information, leaving a final set of 39 patients.

We initially extracted a total of 30 original features as follows: Alanine (Ala), Aspartate (Asp), γ-aminobutyric Acid (GABA), Glutamine (Gln), Glutamate (Glu), Glu + Gln (Glx), Creatine (Cr), Phosphocreatate (PCr), Cr + PCr (tCr), Lactate (Lac), 2-hydroxyglutarate (2HG), N-Acetyl-aspartate (NAA), N-Acetyl-aspartyl-glutamate (NAAG), NAA + NAAG (tNAA), Taurine (Tau), scyllo-Inositol (sI), myo-Inositol (mI), Glycine (Gly), mI + Gly, Glutathione (GSH), Glycerophosphocholine (GPC), Phosphocholine (PCh), GPC + PCh (tCho), Cystathionine (Cystat), creatine singlet around 3.94 ppm ($CrCH_2$), lipids with mean frequencies at 0.89 ppm (Lip09), 1.28 ppm (Lip13a, Lip13b, and Lip13 = Lip13a + Lip13b), 2.04, 2.25, and 2.80 ppm (Lip20).

Due to the limited spectral resolution, we followed standard practice in the field by retaining composite metrics (specifically Glx, tCr, tNAA, mI + Gly, tCho, and Lip13) while excluding their individual components (e.g., Gln, Glu, Cr, PCr, etc.),

Table 1
In vivo MRS biomarkers for gliomas.

Metabolite	Effect	Sample size	Modality	Cross center	Cross modality	Source
GSH ($P = 0.019$), 2HG ($P < 0.001$), Glx ($P = 0.024$), tCho ($P = 0.006$)	Subtyping IDH (mutant/wildtype)	Total: 18 patients, Mutant: 11, Wildtype: 7	9.4T MRS (Siemens)	Single center	None	Bisdas et al. [4]
Ala ($P = 0.0008$), mI ($P = 0.007$)	Subtyping IDH (mutant/wildtype)	Total: 26 patients, Mutant: 20, Wildtype: 6	3T MRS (Siemens)	Single center	None	Alcicek et al. [5]
Glx/tCr ($P < 0.005$)	Grading (LGG/HGG)					
2HG, Glx	Subtyping IDH (mutant/wildtype)	Total: 44 patients, Mutant: 6, Wildtype: 38	3T MRS (GE)	Single center	None	Natsumeda et al. [6]
Cystat	Subtyping 1p/19q (codeletion/non-codeletion)	Total: 65 patients, gene analyzed: 33	3T MRS (Siemens)	2 hospitals	LC-MS, GC-MS, qPCR analyses	Branzoli et al. [7]
		Total: 15 patients		Single center	500 MHz NMR spectrometer	Branzoli et al. [8]
mI ($P = 0.005$)	Diagnosing (gliomas/healthy)	Total: 56 patients	3T MRS (Siemens)	Single center	None	Hattingen et al. [9]
Cho, mI	Typing (glioblastomas/other gliomas)	Total: ~319, Patients: 19, Healthy: ~300	2T MRS (Siemens)	Single center	None	Frahm et al. [10]
mI/Cr, Cho/Cr	Grading (LGG/HGG)	Total: 39, Patients: 34, Healthy: 5	1.5T MRS (not mentioned)	Single center	None	Castillo et al. [11]
Lac, Lac/Cr	Subtyping IDH (mutant/wildtype)	Total: 30 patients, Mutant: 23, Wildtype: 7	3T MRS (not mentioned)	Single center	None	Wenger, K. J. et al. [12]
Cr, PCr	Diagnosis (gliomas/healthy)	Total: 33, Patients: 16, Healthy: 17	1.5T MRS (not mentioned)	Single center	None	Esteve et al. [13]
Gly/2HG ($P < 0.0001$)	Shorter survival with a high Gly/2HG in HGG	Total: 35 patients	3T MRS (Philips)	Single center	None	Tiwari et al. [14]
tCr	Predictor for tumor progression and for malignant tumor transformation	Total: 45 patients	1.5T MRS (Philips), 3T MRSI (Siemens)	Single center	None	Hattingen et al. [15]
Cho/Cr ($P = 0.007$), NAA/Cr ($P = 0.009$)	Grading (LGG/HGG)	Total: 25 patients, 6 LGG, 19 HGG	1.5T MRS (Siemens)	Single center	None	Yerli et al. [16]
Cho/NAA	Marginal delineation	Total: 18 patients, 7 LGG, 11HGG	3T MRSI (Siemens)	Single center	Immunohistochemical staining	Guo et al. [17]
NAA ($P < 0.01$), Cho ($P < 0.01$), Glx ($P < 0.01$)	Diagnosing (oligodendrogliomas/healthy)	Total: 15 patients, 7 LGG, 8 HGG	1.5T MRSI (Siemens)	1 medical center, 2 hospitals	None	Rijpkema et al. [18]

Note: In modality, MRS refers to single voxel magnetic resonance spectroscopy (SVS), and MRSI refers to chemical shift magnetic resonance imaging (CSI). GC: Gas chromatography, LC: Liquid chromatography, MS: Mass spectrometry, qPCR: Quantitative polymerase chain reaction, LGG: Low-grade glioma, HGG: High-grade glioma.

Table 2
Non-MRS *ex-vivo* researches exploiting biomarkers of gliomas.

Metabolite	Effect	Sample size	Modality	Cross center	Cross modality	Source
2HG	Subtyping IDH (mutant/wildtype)	Total: ~1000 patients, 973 myeloid hematologic malignancy, 20 samples of IDH1/2 coding regions for full-length sequencing, 8 thyroid cancer, 2 lymphoma	GC-MS	3 centers: New York, Philadelphia, Boston	None	Ward et al. [19]
2HG, mI, sI, Gly, NAA, NAAG	Subtyping IDH (mutant/wildtype)	Total: 224 patients, Glioblastoma: 162, Astrocytoma: 31, Oligodendroglioma: 31	GC-MS, LC-MS	Single center	None	Björkblom et al. [20]
NAA ($P = 0.049$), NAAG ($P = 0.019$), GSH ($P < 0.001$)	Subtyping IDH (mutant/wildtype)	6 oligodendroglioma cell clone groups, 26 gliomas	LC-MS/MS, GC-MS	2 medical centers, 1 Inc.	Independent LC-MS/MS experiment verifying NAA and NAAG levels	Reitman et al. [21]
Ala ($P < 0.0001$)	Diagnosing (gliomas/healthy)	Total: 42, Patients: 9 LGG, 17 HGG, Healthy: 16	600 MHz NMR spectrometer	Single center	None	Firdous et al. [22]
Gln	Diagnosing (high level of Gln synthetase expression and intra-cell Gln biosynthesis are linked to gliomas)	7 glioblastomas patients, 209 glioblastoma tissue microarrays, several mice, 6 glioblastoma cell lines	7T NMR spectrometer	3 centers: Norway, Luxembourg, UK	(1) HPLC-MS, (2) Immunohistochemical staining, (3) 13C/15 N metabolite tracing, (4) qPCR	Tardito et al. [23]
Gly	Diagnosing (glioblastomas/healthy)	Total: 65 patients, Glioblastoma: 24, Other tumor: 41	600 MHz NMR spectrometer	Single center	None	Wright et al. [24]
Lac, Glu	Distinguish the HGG and the peritumor	Total: 15 patients, Glioblastoma: 14, Astrocytoma: 1	CMA 70, CMA 600	Single center	In-vitro experiment of the recovery	Roslin et al. [25]
Tau	Grading (LGG/HGG)	Total: 31 patients, Mutant: 6, Wildtype: 25	MSI	Single center	HE staining	Kampa et al. [26]
Tau	Grading (LGG/HGG)	Total: 69 patients, Grade II: 18, Grade III: 18, Grade IV: 33,	UHPLC/MS-MS, GC/MS	Single center	(1) Western blot analysis, (2) Immunohistochemical staining,	Prabhu et al. [27]

Note: GC: Gas chromatography, LC: Liquid chromatography, MS: Mass spectrometry, MSI: Mass spectrometry imaging, HP: High performance, qPCR: Quantitative polymerase chain reaction, NMR: Nuclear magnetic resonance, LGG: Low-grade glioma, HGG: High-grade glioma.

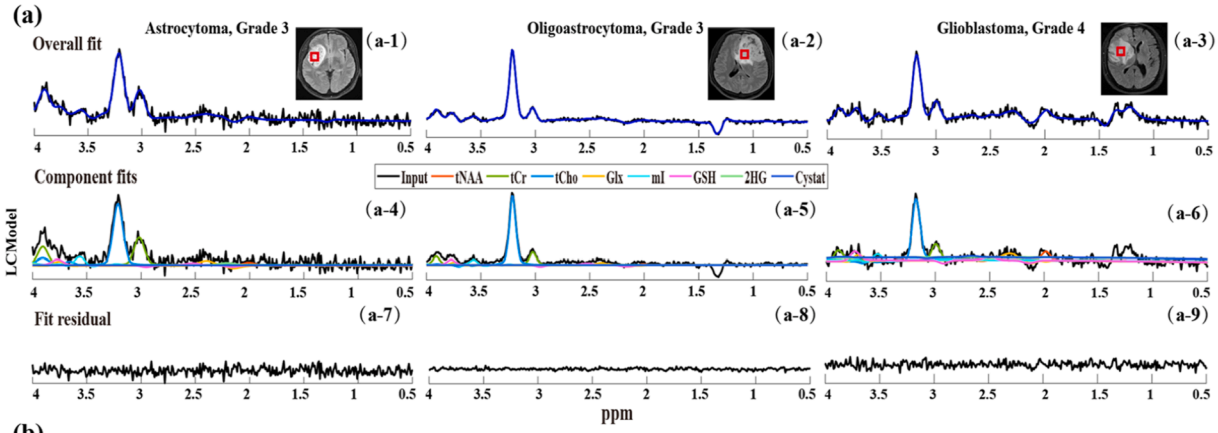

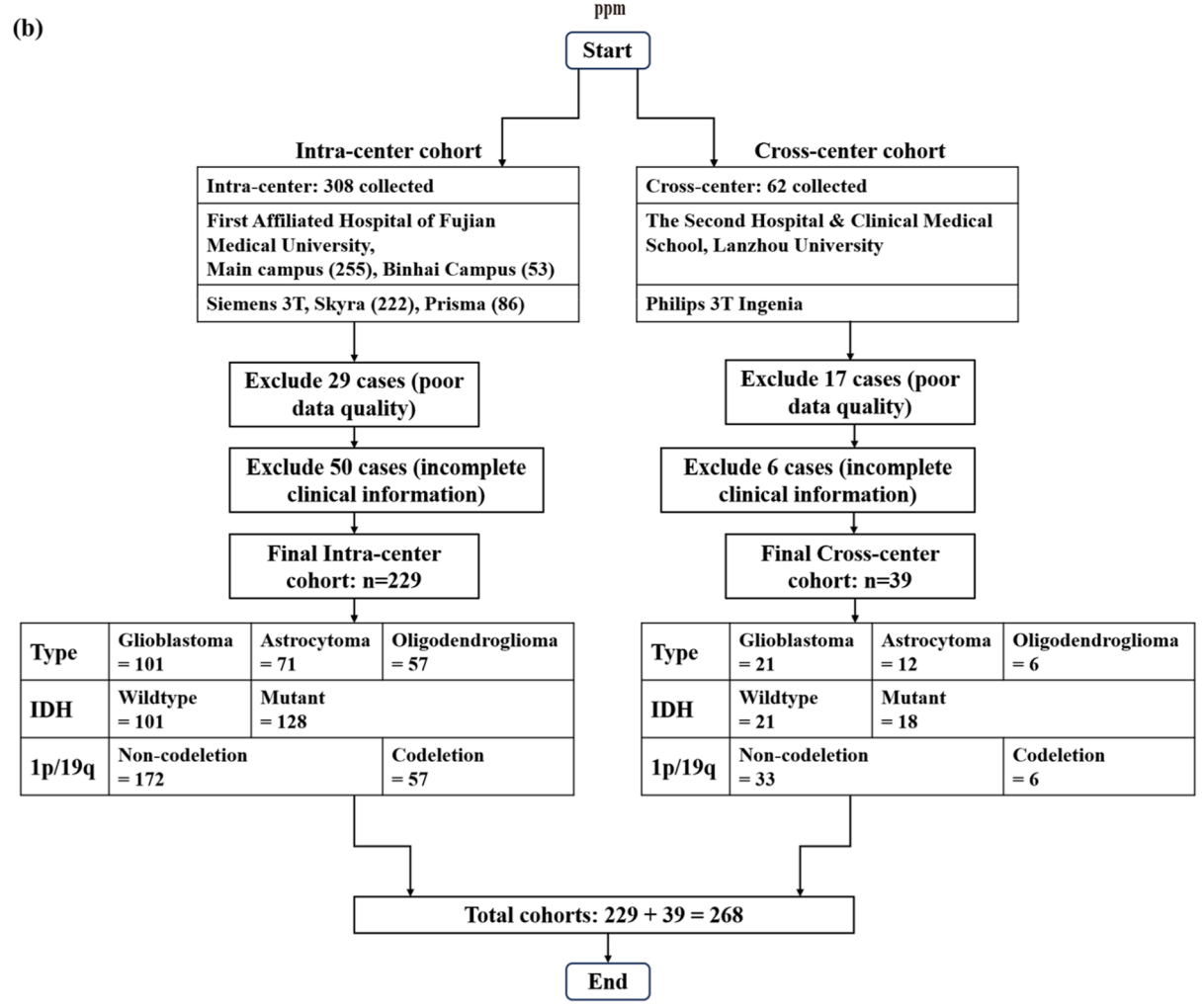

Fig. 1. Dataset. (a) Typical quantitative results for each type of adult diffuse glioma, (b) Glioma data collection, including molecular profiling.

which resulted in a refined set of 18 individual features for subsequent analysis. Furthermore, to mitigate concentration variability and enhance robustness, we adopted the ratios of other metabolite concentrations to the relatively high and stable concentrations of tCho, tCr, and tNAA as the input features [30]. Specifically, among the 18 refined features, tCho, tCr, and tNAA were designated as the reference denominators. The remaining 15 metabolite concentrations—namely, Ala, Asp, GABA, Glx, Lac, 2HG, Tau, sI, mI + Gly, GSH, Cystat, $CrCH_2$, Lip09, Lip13, and Lip20—were each divided by the concentrations of tCho, tCr, and tNAA, yielding 45 ratio features (15 metabolites × 3 reference). These 45 ratios were then concatenated

with the original concentrations of the three reference metabolites (tCr/tCho, tNAA/tCho, tNAA/tCr) to retain their absolute quantitative information, producing a final feature vector of 48 dimensions ($15 \times 3 + 3$) (see Table S2).

Our task is to perform molecular subtyping of IDH and 1p/19q based on the relative concentrations. Data-driven analysis is performed via Partial Least Square-Discrimination Analysis (PLS-DA) [31] on MATLAB platform (See Appendix A. Supplementary data Chap. 6 for the used functions and parameter configuration).

For IDH classification, mutant is positive and wildtype is negative. For 1p/19q classification, codeletion is positive and non-codeletion is negative. True positive (TP), true negative (TN), false positive (FP), and false negative (FN) are specifically defined in Appendix A. Supplementary data Tables S5 and S6. Accuracy, sensitivity, specificity, Youden's index, and Cohen's kappa are defined as:

$$\text{accuracy} = (\text{TP} + \text{TN}) / (\text{TP} + \text{FP} + \text{TN} + \text{FN}),$$

$$\text{sensitivity} = \text{TP} / (\text{TP} + \text{FN}),$$

$$\text{specificity} = \text{TN} / (\text{TN} + \text{FP}),$$

$$\text{Youden}'\text{s index} = \text{sensitivity} + \text{specificity} - 1,$$

$$\textit{Cohen's } \kappa\textit{appa} = \frac{2(\text{TP} \times \text{TN} - \text{FP} \times \text{FN})}{(\text{TP} + \text{FP})(\text{FP} + \text{TN}) + (\text{TP} + \text{FN})(\text{FN} + \text{TN})}$$

Receiver operating characteristic (ROC) curve [32] and area under the curve (AUC) [33] are the most commonly used indicators to evaluate trained classifiers. Higher AUC reflects better separability of the feature space. The training and testing sets were split in the ratio of 4:1 with 200 different random seeds from 1 to 200 without manual selection.

To circumvent the biases inherent in heuristic thresholding, we implemented a performance-driven feature selection strategy designed to identify the most parsimonious and robust metabolic signatures. The selection process was conducted in three stages: (1) feature prioritization—all 48 candidate features were ranked based on their Variable Importance in Projection (VIP) scores [34], stabilized via averaging over 200 random iterations; (2) iterative optimization—a forward selection approach was employed, iteratively adding features and evaluating the cumulative impact on four performance dimensions, namely, the minimum of sensitivity and specificity, overall accuracy, Cohen's kappa, and AUC; (3) objective selection: the optimal feature set was determined by identifying the elbow point—the inflection point where performance metrics plateaued and additional features yielded diminishing marginal returns. To mitigate multicollinearity and eliminate redundancy within the elbow-derived subset, we performed hierarchical clustering based on distance correlation (dCorr) [35]. The feature exhibiting the highest mean intra-cluster correlation was retained as the representative for each cluster, ensuring the final model consisted of metabolically independent and statistically significant predictors.

3. Results

3.1. Performance-driven feature selection

A forward cumulative feature selection process based on classification performance was utilized. We calculated VIP scores over 200 random repetitions (Figs. 2 and 3) to establish a preliminary rank. Starting with the highest-ranking feature, we iteratively added features and evaluated four metrics: (a) minimum of sensitivity and specificity, (b) accuracy, (c) Cohen's Kappa, and (d) AUC (Figs. 4 and 5).

The optimal number of features was determined by the elbow area—where performance reached a plateau (yellow background in Figs. 4 and 5). This method ensures the selection is driven by statistical gain rather than manual intervention. To prevent the selected elbow features from becoming redundant variations of the same metabolites and instead ensure they represent distinct biological axes, we performed hierarchical clustering on every elbow feature set (17~21 features for IDH, and 23–32 features for 1p/19q) to remove redundancy. From each cluster, we selected the feature with the highest average correlation to others in that cluster as the representative. Interestingly, this yielded 9 features for IDH and 12 for 1p/19q (Figs. 6 and 7), which represented the maximal common intersection across all feature sizes in the elbow regions, respectively. This convergence confirms that these specific 9 and 12 features are the core consensus drivers of the classification model.

3.2. Classification performance

Our representative-feature model demonstrated superior robustness compared to both single-biomarker baselines and all-feature model. For example, for IDH classification in cross-center validation, while the single-metabolite model (2HG alone) exhibited AUC<0.61, the representative-feature model significantly improved discrimination with AUC>0.85 (See Table 3 for IDH and Table 4 for 1p/19q). Compared with the all-feature model, the representative-feature model gave a comparable classification performance (Table 3 for IDH, Table 4 for 1p/19q) but with the model size significantly reduced. To evaluate the rationality of the discriminant model, calibration curve analysis [36] was employed. A calibration curve

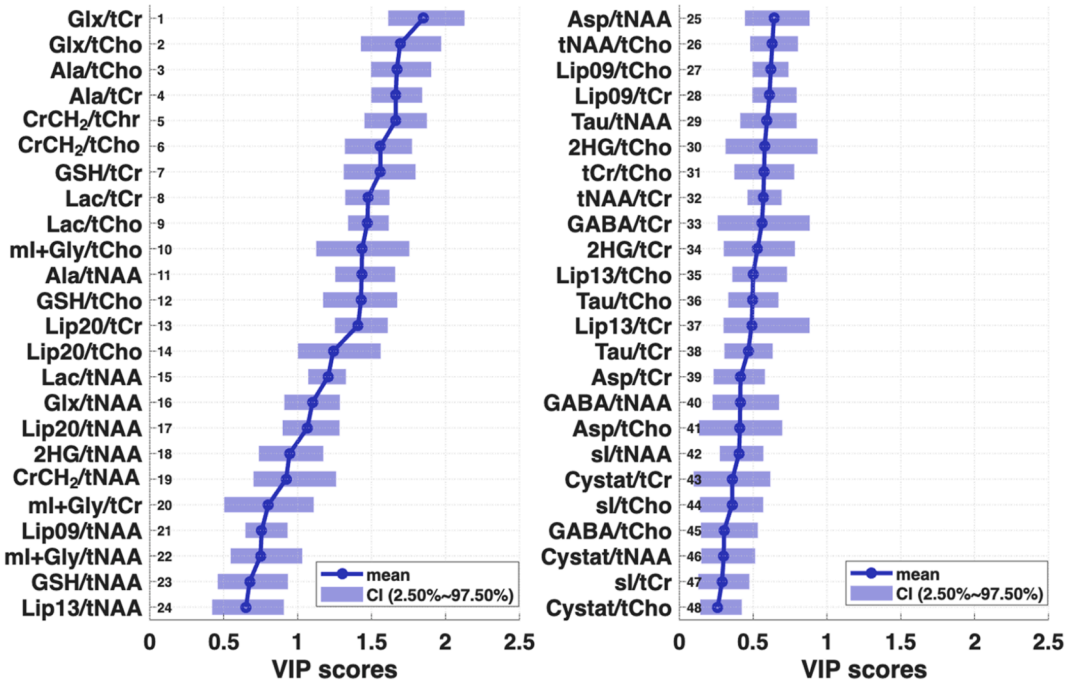

Fig. 2. Average VIP scores of all 48 features for IDH prediction, sorted in descending order (averaged over 200 random repetitions). The line shows the mean of VIP scores, and the box shows the confidence interval (2.5th–97.5th percentile). Note: The numbers 1-48 represent the ranking order of the average VIP scores.

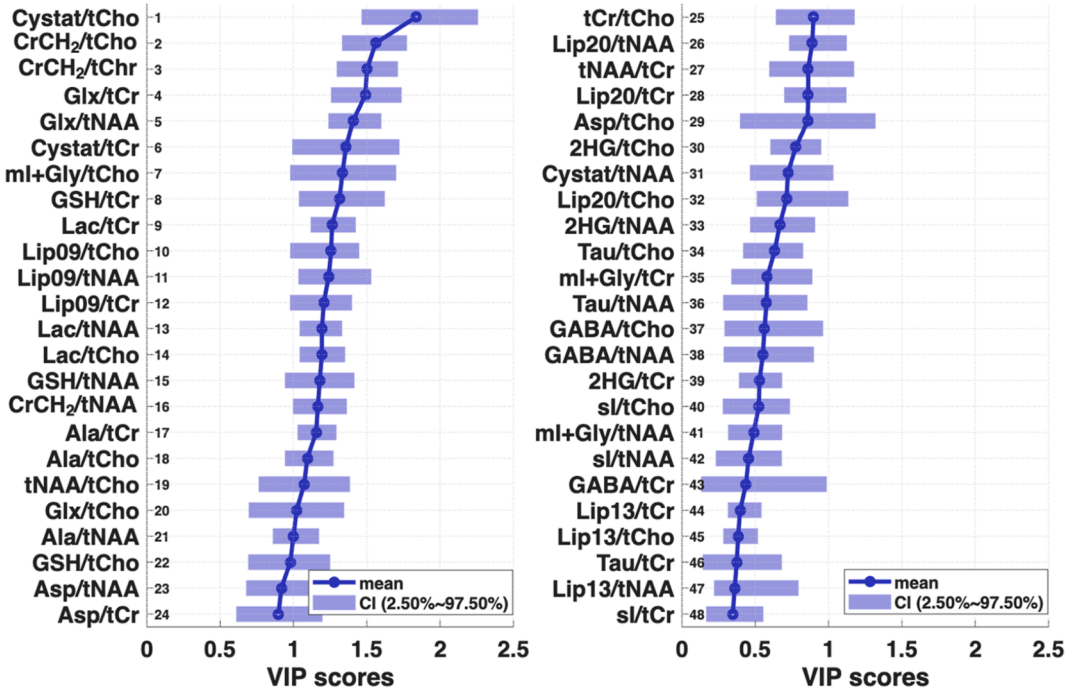

Fig. 3. Average VIP scores of the 48 features for 1p/19q prediction, sorted in descending order (averaged over 200 random repetitions). The line shows the mean of VIP scores, and the box shows the confidence interval (2.5th–97.5th percentile). Note: The numbers 1-48 represent the ranking order of the average VIP scores.

graphically assesses how well the predicted probabilities align with the actual observed outcomes. In this plot, the x-axis represents the model-predicted positive probability and the y-axis shows the corresponding observed proportion. Perfect calibration corresponds to the 45° diagonal line, where the predicted probability equals the observed probability at every point. Calibration curves for Intra-center and Cross-center are shown in Figs. 8 and 9 for IDH and 1p/19q discriminant model,

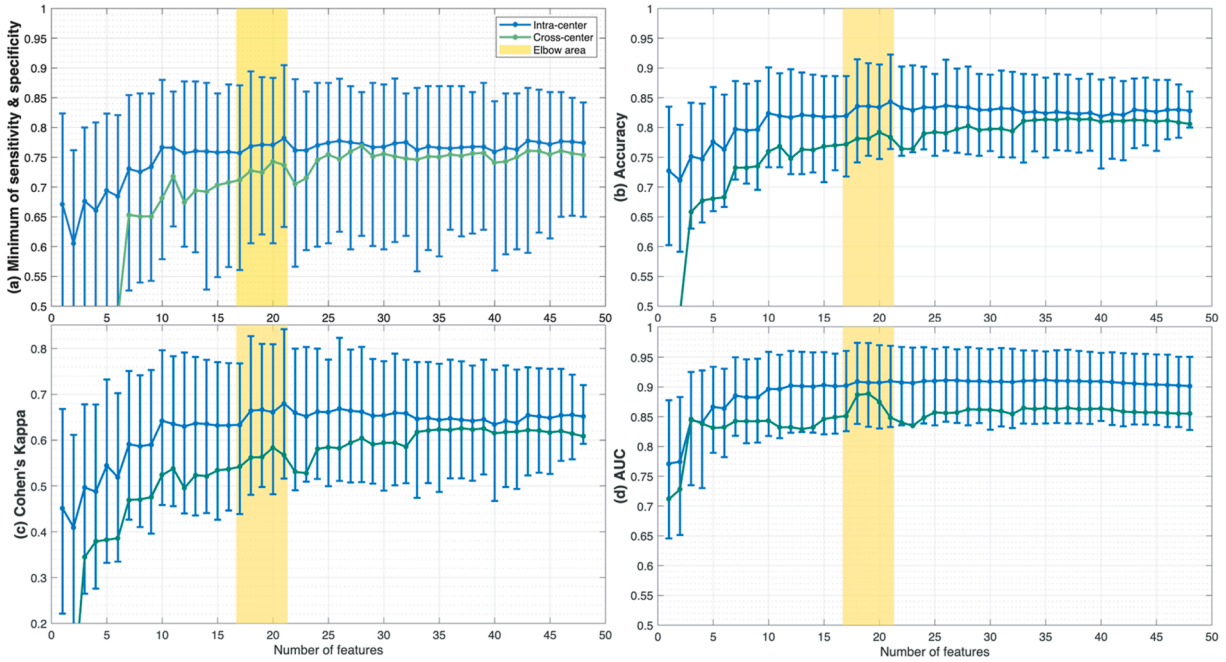

Fig. 4. IDH cumulative feature classification performance. (a) Minimum of sensitivity and specificity, (b) accuracy, (c) Cohen's kappa, and (d) AUC. The line shows the mean, and the bar shows the confidence interval (2.5th–97.5th percentile). The area marked by yellow background is elbow area (17–21 features) where the classification performances come to a plateau onset and stop gaining large progress.

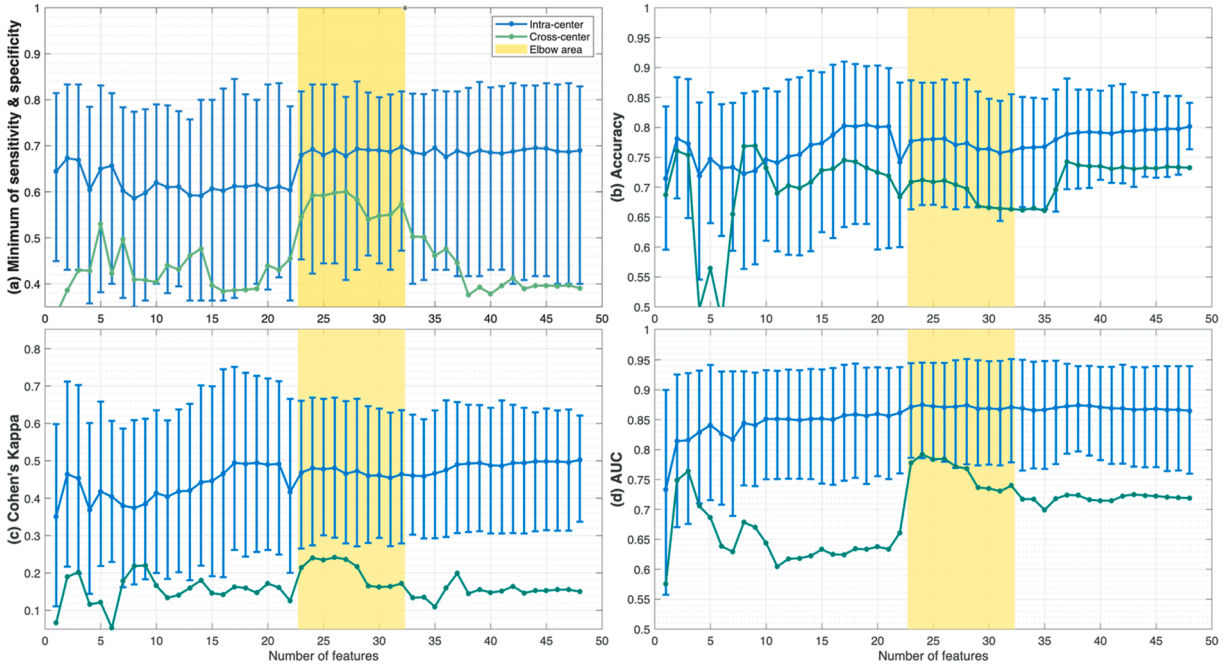

Fig. 5. 1p/19q cumulative feature classification performance. (a) Minimum of sensitivity and specificity, (b) accuracy, (c) Cohen's kappa, and (d) AUC. The line shows the mean, and the bar shows the confidence interval (2.5th–97.5th percentile). The area marked by yellow background is elbow area (23–32 features) where the classification performances come to a plateau onset and stop gaining large progress.

respectively. We employed Locally Weighted Scatterplot Smoothing (LOWESS) [37] to plot calibration curves. The close alignment of the curves with the ideal diagonal line indicates excellent model calibration and generalizability. The low Brier scores [38] (IDH: 0.1205 intra-center/0.1567 cross-center; 1p/19q: 0.1232 intra-center/0.1580 cross-center) quantitatively confirm that the model is well-calibrated and not overfitting the training data.

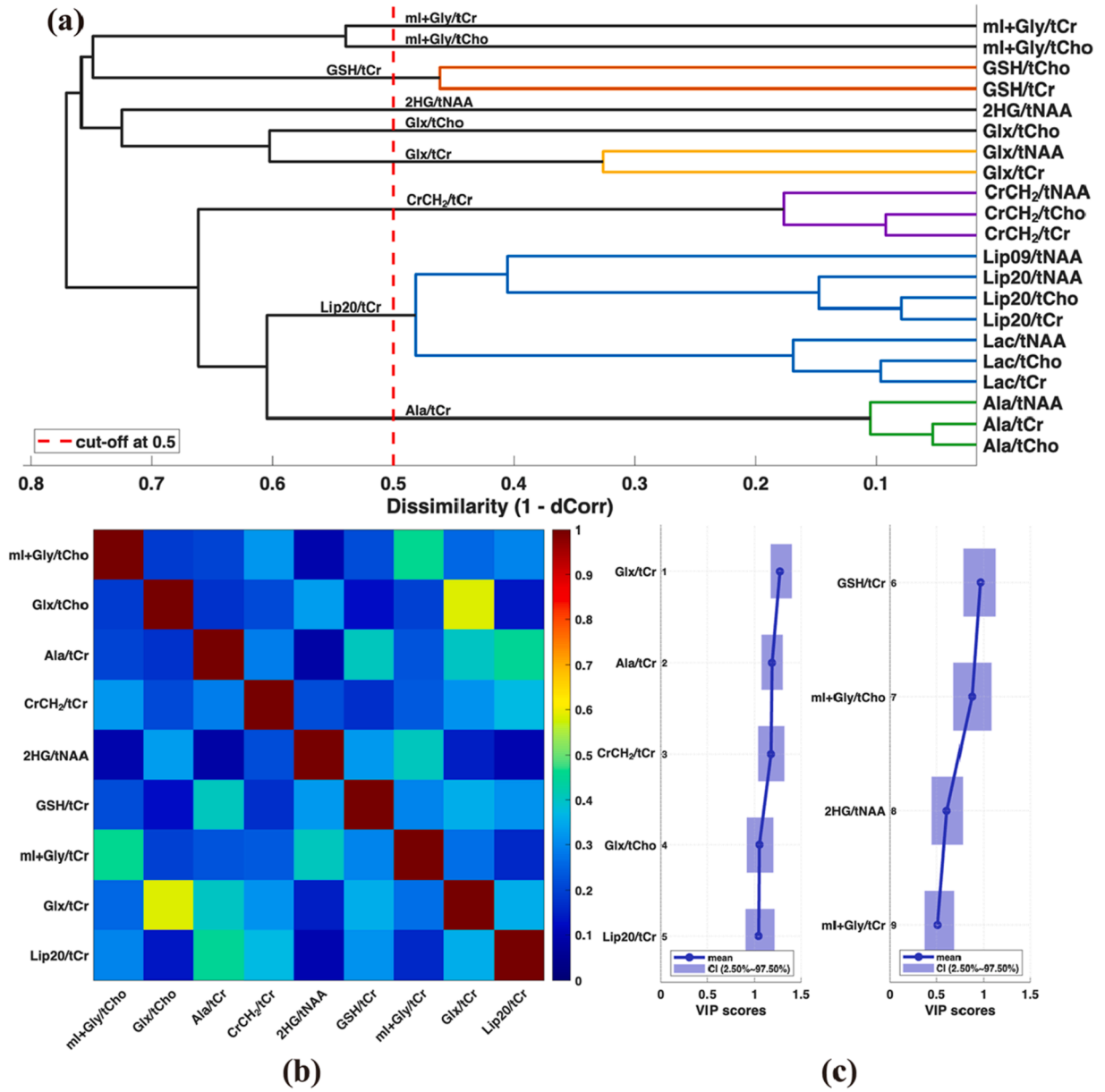

Fig. 6. Hierarchical clustering results for IDH classification. (a) Hierarchical dendrogram, (b) distance correlation heatmap, (c) VIP scores over 200 repetitions. Note: The 9 features were derived from a 21-feature set. Within the elbow region (17–21 features; see Fig. 4), the representative subsets obtained by hierarchical clustering all contained the maximal common intersection. Thus, only the clustering result for the 21-feature set is shown. Features: (1) Glx/tCr, (2) Ala/tCr, (3) $CrCH_2$/tCr, (4) Glx/tCho, (5) Lip20/tCr, (6) GSH/tCr, (7) (mI + Gly)/tCho, (8) 2HG/tNAA, (9) (mI + Gly)/tCr, ranked in descending order by VIP score.

To validate the robustness of our PLS-DA framework, we benchmarked it against Support Vector Machine (SVM) and Random Forest (RF) classifiers. Models were evaluated on both the full 48-feature set and the reduced feature sets identified by our performance-driven strategy. Furthermore, to quantify the practical gain of our multivariate approach, we established a baseline using single-metabolite models (specifically 2HG for IDH and Cystathionine for 1p/19q) normalized against internal references (tCho, tCr, tNAA). This comparison explicitly demonstrated the added value of integrating multiple metabolic features beyond known single biomarkers. The detailed information is shown in Tables S3 and S4.

4. Limitations and future work

It is important to note that this study utilized single-voxel MRS, with voxels localized specifically to the enhancing tumor core. Consequently, the predictive model is designed to reflect the molecular status of the core tumor phenotype. Diffuse gliomas are characterized by extensive infiltration and spatial heterogeneity [39]; therefore, the metabolic signatures of the

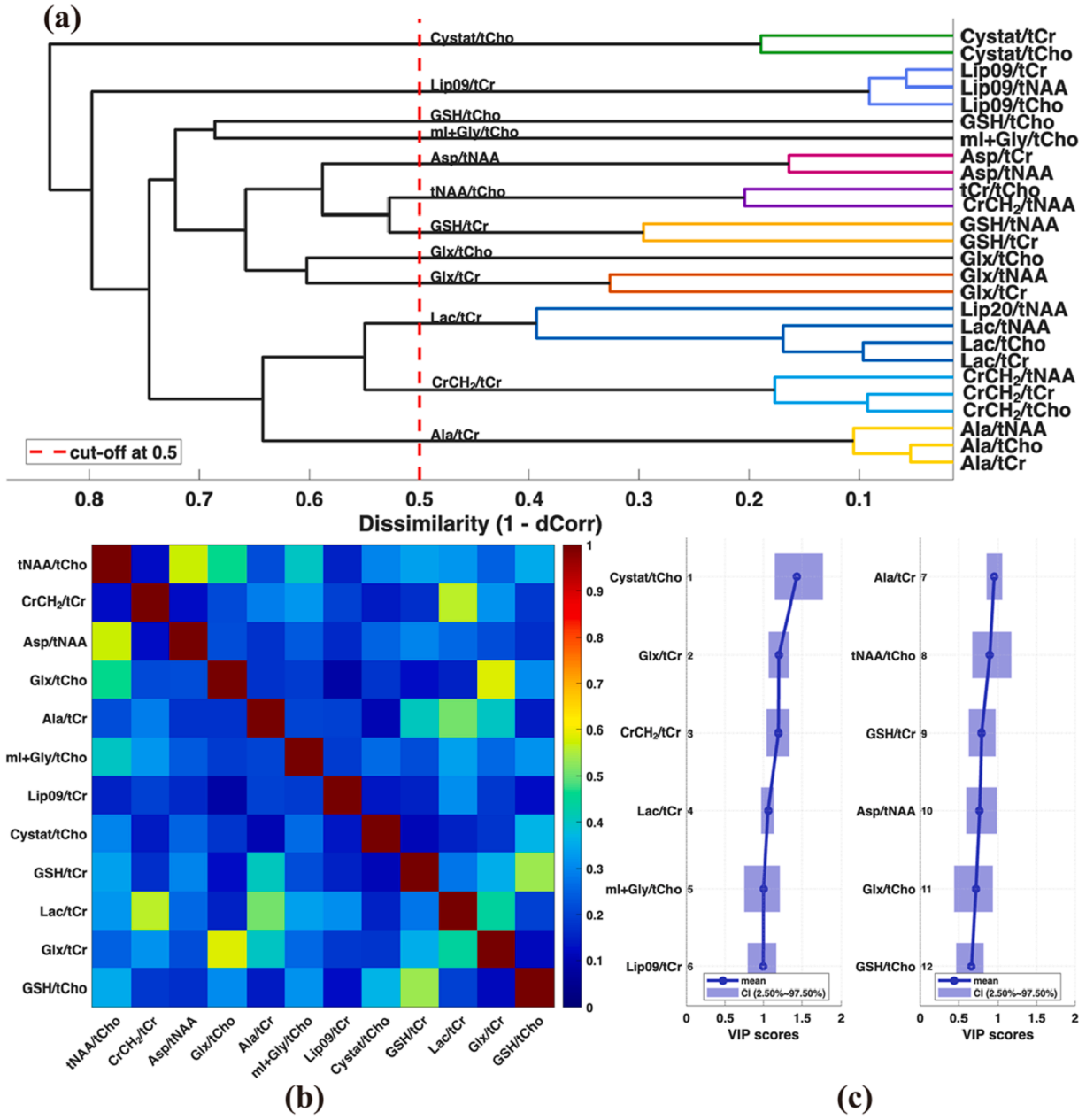

Fig. 7. Hierarchical clustering results for 1p/19q classification. (a) Hierarchical dendrogram, (b) distance correlation heatmap, (c) VIP scores over 200 repetitions. Note: The 12 features were derived from a 26-feature set. Within the elbow region (23–32 features; see Fig. 5), the representative subsets obtained by hierarchical clustering all contained the maximal common intersection. Thus, only the clustering result for the 26-feature set is shown. Features: (1) Cystat/tCho, (2) Glx/tCr, (3) $CrCH_2$/tCr, (4) Lac/tCr, (5) (ml + Gly)/tCho, (6) Lip09/tCr, (7) Ala/tCr, (8) tNAA/tCho, (9) GSH/tCr, (10) Asp/tNAA, (11) Glx/tCho, (12) GSH/tCho, ranked in descending order by VIP score.

peritumoral region may differ substantially from those of the core [40]. Consequently, our current study focuses on the metabolic profile of the tumor core to establish a robust and reproducible signature for non-invasive genotyping. Future studies include validating these findings using multi-voxel MRS or MR Spectroscopic Imaging (MRSI) [41], which would allow for a comprehensive assessment of metabolic heterogeneity across the entire lesion and its margins.

Furthermore, we plan to collect more cross-center data in the future, with a particular emphasis on balancing the sample sizes between 1p/19q codeleted and non-codeleted cohorts. Looking ahead, a key objective is the deployment of our model onto a cloud-native MRS ecosystem [42]. By interfacing with the platform's established intelligent quantification modules [43–45], we envision an end-to-end solution that transforms raw spectral data into actionable genotypic insights, thereby advancing precision diagnostics for glioma patients.

Table 3
IDH prediction performance on 200 random repetitions.

Dataset	Feature	Accuracy	Sensitivity	Specificity	Youden's index	Cohen's kappa	AUC
Intra	Representative	**0.843** (0.814–0.878)	**0.862** (0.733–0.963)	**0.817** (0.650–0.977)	**0.679** (0.592–0.758)	**0.679** (0.612–0.755)	**0.906** (0.845–0.965)
	2HG	0.671 (0.643–0.706)	0.826 (0.660–0.966)	0.467 (0.235–0.684)	0.294 (0.183–0.392)	0.303 (0.203–0.393)	0.687 (0.563–0.784)
	All	0.828 (0.800–0.860)	0.841 (0.711–0.957)	0.813 (0.650–0.949)	0.654 (0.582–0.730)	0.652 (0.592–0.720)	0.902 (0.828–0.951)
Cross	Representative	0.796 (0.769–0.846)	0.812 (0.694–0.889)	0.783 (0.714–0.905)	0.595 (0.528–0.683)	0.592 (0.532–0.688)	**0.857** (0.840–0.873)
	2HG	0.561 (0.539–0.615)	**0.852** (0.778–0.944)	0.312 (0.191–0.429)	0.163 (0.119–0.262)	0.156 (0.114–0.253)	0.603 (0.595–0.612)
	All	**0.806** (0.744–0.846)	0.767 (0.611–0.889)	**0.840** (0.714–0.905)	**0.606** (0.484–0.698)	**0.608** (0.484–0.693)	0.855 (0.831–0.877)

Note: Figures are shown by mean and confidence interval (2.5th ~ 97.5th percentiles). Classifiers are trained on Intra-center dataset with training and testing in the ratio of 4:1. Representative features: (1) Glx/tCr, (2) Ala/tCr, (3) $CrCH_2$/tCr, (4) Glx/tCho, (5) Lip20/tCr, (6) GSH/tCr, (7) (ml + Gly)/tCho, (8) 2HG/tNAA, (9) (ml + Gly)/tCr, ranked in descending order by VIP score (Fig. 6(c)). 2HG feature: (1) 2HG/tCho, (2) 2HG/tCr, (3) 2HG/tNAA. All feature: all 48 features (See Table S2). Bold numbers indicate optimal performances.

Table 4
1p/19q prediction performance on 200 random repetitions.

Dataset	Feature	Accuracy	Sensitivity	Specificity	Youden's index	Cohen's kappa	AUC
Intra	Representative	0.778 (0.745–0.819)	0.727 (0.472–0.923)	0.794 (0.704–0.895)	0.521 (0.331–0.670)	0.459 (0.318–0.568)	0.858 (0.785–0.930)
	Cystat	0.692 (0.659–0.733)	**0.757** (0.500–1.000)	0.671 (0.594–0.750)	0.430 (0.229–0.619)	0.334 (0.203–0.447)	0.732 (0.600–0.845)
	All	**0.801** (0.763–0.841)	0.723 (0.400–1.000)	**0.827** (0.729–0.956)	**0.550** (0.327–0.719)	**0.503** (0.337–0.621)	**0.865** (0.760–0.939)
Cross	Representative	0.711 (0.641–0.795)	**0.642** (0.333–1.000)	0.723 (0.606–0.879)	**0.365** (0.091–0.667)	**0.242** (0.071–0.381)	**0.787** (0.747–0.828)
	Cystat	0.594 (0.564–0.615)	0.416 (0.333–0.500)	0.626 (0.576–0.667)	0.042 (−0.046 to 0.136)	0.024 (−0.029 to 0.085)	0.614 (0.593–0.621)
	All	**0.732** (0.641–0.769)	0.391 (0.167–0.500)	**0.795** (0.697–0.848)	0.185 (−0.015 to 0.348)	0.150 (−0.014 to 0.307)	0.719 (0.659–0.763)

Note: Figures are shown by mean and confidence interval (2.5th ~ 97.5th percentiles). Classifiers are trained on Intra-center dataset with training and testing in the ratio of 4:1. Representative features: (1) Cystat/tCho, (2) Glx/tCr, (3) $CrCH_2$/tCr, (4) Lac/tCr, (5) (ml + Gly)/tCho, (6) Lip09/tCr, (7) Ala/tCr, (8) tNAA/tCho, (9) GSH/tCr, (10) Asp/tNAA, (11) Glx/tCho, (12) GSH/tCho, ranked in descending order by VIP score (Fig. 7(c)). Cystat feature: (1) Cystat/tCho, (2) Cystat/tCr, (3) Cystat/tNAA. All feature: all 48 features (See Table S2). Bold numbers indicate optimal performances.

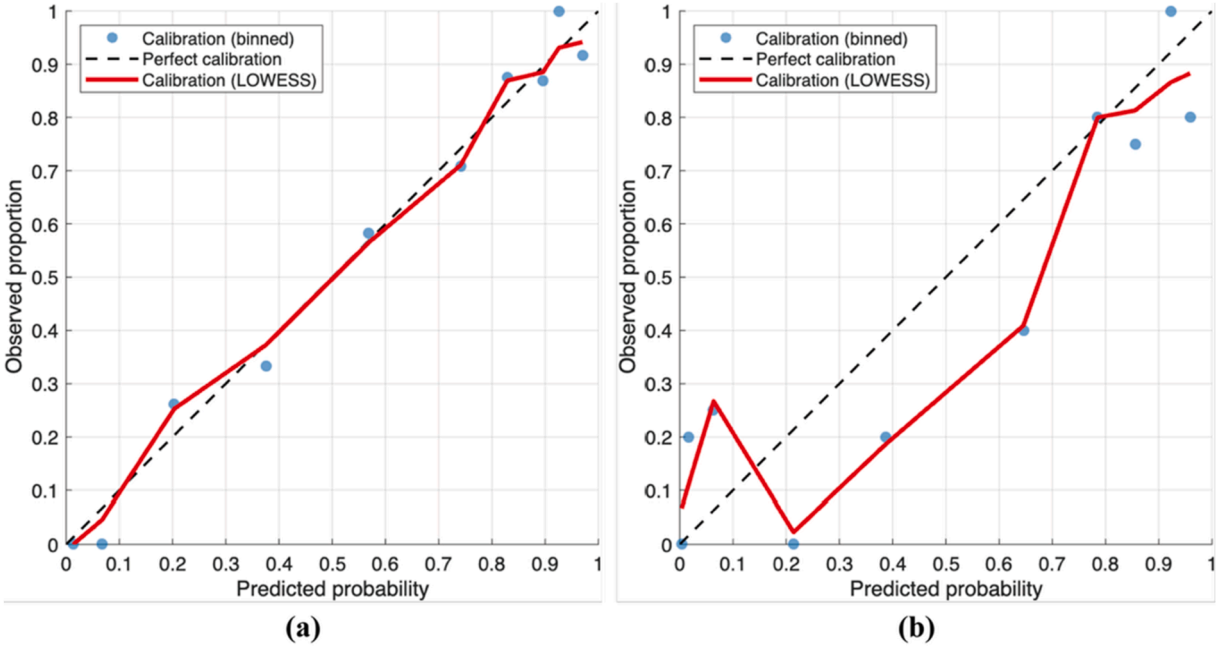

Fig. 8. Calibration curves of IDH representative-feature classification model. (a) Intra-center, (b) Cross-center. Brier (Intra) = 0.1205, Brier (Cross) = 0.1567. LOWESS method is employed for the red curves. Features: (1) Glx/tCr, (2) Ala/tCr, (3) $CrCH_2$/tCr, (4) Glx/tCho, (5) Lip20/tCr, (6) GSH/tCr, (7) (ml + Gly)/tCho, (8) 2HG/tNAA, (9) (ml + Gly)/tCr, ranked in descending order by VIP score.

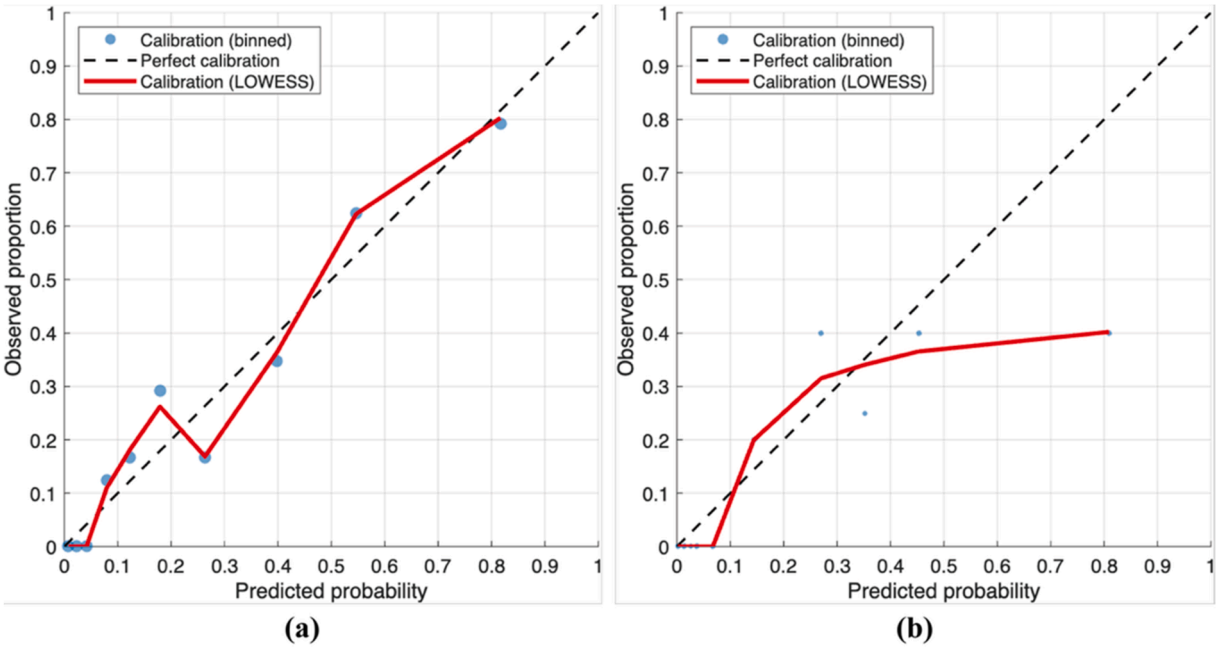

Fig. 9. Calibration curves of 1p/19q representative-feature classification model. (a) Intra-center, (b) Cross-center. Brier (Intra) = 0.1232, Brier (Cross) = 0.1580. The LOWESS method is employed for the red curves. Features: (1) Cystat/tCho, (2) Glx/tCr, (3) $CrCH_2$/tCr, (4) Lac/tCr, (5) (mI + Gly)/tCho, (6) Lip09/tCr, (7) Ala/tCr, (8) tNAA/tCho, (9) GSH/tCr, (10) Asp/tNAA, (11) Glx/tCho, (12) GSH/tCho, ranked in descending order by VIP score.

5. Conclusions

This study presents a non-invasive, MRS-based metabolic profiling framework for molecular subtyping of adult diffuse gliomas. By assembling the largest cross-center, cross-vendor MRS dataset for this purpose ($n = 268$), we moved beyond single-biomarker strategies to systematically evaluate 48 features from 19 metabolites and ranked their importances. Through a performance-driven feature selection pipeline, robust metabolic signatures—9 features for IDH and 12 for 1p/19q—were identified that outperformed conventional single-metabolite baselines (2HG for IDH and Cystat for 1p/19q). The resulting integrated models achieved strong and generalizable performance, with intra-center/cross-center AUCs of 0.906/0.857 for IDH status and 0.858/0.787 for 1p/19q codeletion status. These findings highlight the synergistic value of multi-metabolite signatures and support the translation of this MRS-based strategy into clinical workflows as a preoperative adjunct for glioma genotyping, potentially reducing reliance on invasive tissue sampling.

CRediT authorship contribution statement

Zhangren Tu: Writing – original draft, Methodology, Investigation, Formal analysis, Conceptualization. **Wanjun Hu:** Methodology, Investigation, Formal analysis, Data curation. **Jialve Zhang:** Writing – original draft, Software, Methodology, Investigation, Formal analysis, Conceptualization. **Zhen Xing:** Data curation. **Jiamin Li:** Data curation. **Jingjing Xu:** Investigation, Formal analysis. **Meijin Lin:** Formal analysis. **Xianwang Jiang:** Formal analysis. **Dairong Cao:** Supervision, Data curation. **Jing Zhang:** Supervision, Data curation. **Di Guo:** Writing – original draft, Supervision, Methodology, Investigation, Funding acquisition, Conceptualization. **Xiaobo Qu:** Writing – original draft, Supervision, Methodology, Investigation, Funding acquisition, Conceptualization.

Data availability

The statistical analysis of the relative quantification results is available in Appendix A. Supplementary data. Due to patient privacy protection regulations, the DICOM files of the MRS data and specific quantification tables cannot be made publicly available.

Ethics approval and consent participate

Intra-Center patient data were approved by the ethics committee (No. MRCTA, ECFAH of FMU [2020] 312) of the First Affiliated Hospital of Fujian Medical University. Cross-Center patient data were approved by the ethics committee (2024A-181) of the Second Hospital & Clinical Medical School, Lanzhou University.

Declaration of competing interest

The authors declare the following financial interests/personal relationships which may be considered as potential competing interests: Xiaobo Qu is an editorial board member of *Magnetic Resonance Letters* but was not involved in the editorial review or the decision to publish this article.

Acknowledgement

This work was supported in part by the National Key R&D Program of China under grant 2023YFF0714200, National Natural Science Foundation of China under grants 62331021 and 62371410, Natural Science Foundation of Fujian Province of China under grants 2023J02005, Zhou Yongtang Fund for High Talents Team under grant 0621-Z0332004, Fujian Provincial Minjiang Scholar Program 405010126002, Lujiang Outstanding Scholar Program at Xiamen University of Technology, and Nanqiang Outstanding Talents Program at Xiamen University. We would like to express our gratitude for the support from the Fujian Provincial Leading Talents in Scientific and Technological Innovation program.

Appendix A. Supplementary data

Supplementary data to this article can be found online at https://doi.org/10.1016/j.mrl.2026.200292.

References

[1] Q.T. Ostrom, G. Cioffi, H. Gittleman, N. Patil, K. Waite, C. Kruchko, J.S. Barnholtz-Sloan, Cbtrus statistical report: primary brain and other central nervous system tumors diagnosed in the United States in 2012–2016, Neuro Oncol. 21 (2019) v1–v100.
[2] B.T. Whitfield, J.T. Huse, Classification of adult-type diffuse gliomas: impact of the world health organization 2021 update, Brain Pathol. 32 (2022) e13062.
[3] S. Cardaci, M.R. Ciriolo, TCA cycle defects and cancer: when metabolism tunes redox state, Int. J. Cell Biol. 1 (2012) 161837.
[4] S. Bisdas, G.L. Chadzynski, C. Braun, J. Schittenhelm, M. Skardelly, G.E. Hagberg, T. Ethofer, R. Pohmann, G. Shajan, J. Engelmann, MR spectroscopy for *in vivo* assessment of the oncometabolite 2-hydroxyglutarate and its effects on cellular metabolism in human brain gliomas at 9.4T, J. Magn. Reson. Imag. 44 (2016) 823–833.
[5] S. Alcicek, U. Pilatus, A. Manzhurtsev, K.J. Weber, M.W. Ronellenfitsch, J.P. Steinbach, E. Hattingen, K.J. Wenger, Amino acid metabolism in glioma: *In vivo* MR spectroscopic detection of alanine as a potential biomarker of poor survival in glioma patients, J. Neuro Oncol. 170 (2024) 451–461.
[6] M. Natsumeda, K. Motohashi, H. Igarashi, T. Nozawa, H. Abe, Y. Tsukamoto, R. Ogura, M. Okada, T. Kobayashi, H. Aoki, Reliable diagnosis of IDH-mutant glioblastoma by 2-hydroxyglutarate detection: a study by 3T magnetic resonance spectroscopy, Neurosurg. Rev. 41 (2018) 641–647.
[7] F. Branzoli, C. Pontoizeau, L. Tchara, A.L. Di Stefano, A. Kamoun, D.K. Deelchand, R. Valabrègue, S. Lehéricy, M. Sanson, C. Ottolenghi, Cystathionine as a marker for 1p/19q codeleted gliomas by *in vivo* magnetic resonance spectroscopy, Neuro Oncol. 21 (2019) 765–774.
[8] F. Branzoli, D.K. Deelchand, M. Sanson, S. Lehéricy, M. Marjańska, *In vivo* ^{1}H MRS detection of cystathionine in human brain tumors, Magn. Reson. Med. 82 (2019) 1259–1265.
[9] E. Hattingen, P. Raab, K. Franz, F.E. Zanella, H. Lanfermann, U. Pilatus, Myo-inositol: a marker of reactive astrogliosis in glial tumors? NMR Biomed. 21 (2008) 233–241.
[10] J. Frahm, H. Bruhn, W. Hänicke, K.-D. Merboldt, K. Mursch, E. Markakis, Localized proton NMR spectroscopy of brain tumors using short-echo time steam sequences, J. Comput. Assist. Tomogr. 15 (1991) 915–922.
[11] M. Castillo, J.K. Smith, L. Kwock, Correlation of myo-inositol levels and grading of cerebral astrocytomas, Am. J. Neuroradiol. 21 (2000) 1645–1649.
[12] K. Wenger, J. Steinbach, O. Bähr, U. Pilatus, E. Hattingen, Lower lactate levels and lower intracellular ph in patients with IDH-mutant versus wild-type gliomas, Am. J. Neuroradiol. 41 (2020) 1414–1422.
[13] F. Esteve, S. Grand, C. Rubin, D. Hoffmann, B. Pasquier, D. Graveron-Demilly, R. Mahdjoub, J.-F. Le Bas, MR spectroscopy of bilateral thalamic gliomas, Am. J. Neuroradiol. 20 (1999) 876–881.
[14] V. Tiwari, E.V. Daoud, K.J. Hatanpaa, A. Gao, S. Zhang, Z. An, S.K. Ganji, J.M. Raisanen, C.M. Lewis, P. Askari, Glycine by MR spectroscopy is an imaging biomarker of glioma aggressiveness, Neuro Oncol. 22 (2020) 1018–1029.
[15] E. Hattingen, P. Raab, K. Franz, H. Lanfermann, M. Setzer, R. Gerlach, F.E. Zanella, U. Pilatus, Prognostic value of choline and creatine in who grade II gliomas, Neuroradiology 50 (2008) 759–767.
[16] H. Yerli, A.M. Agildere, Ö. Özen, E. Geyik, B. Atalay, A.H. Elhan, Evaluation of cerebral glioma grade by using normal side creatine as an internal reference in multi-voxel ^{1}H-MR spectroscopy, Diagn. Interv. Radiol. 13 (2007) 3.
[17] J. Guo, C. Yao, H. Chen, D. Zhuang, W. Tang, G. Ren, Y. Wang, J. Wu, F. Huang, L. Zhou, The relationship between Cho/NAA and glioma metabolism: implementation for margin delineation of cerebral gliomas, Acta Neurochir. 154 (2012) 1361–1370.
[18] M. Rijpkema, J. Schuuring, Y. van der Meulen, M. van der Graaf, H. Bernsen, R. Boerman, A. Van Der Kogel, A. Heerschap, Characterization of oligodendrogliomas using short echo time ^{1}H MR spectroscopic imaging, NMR Biomed. 16 (2003) 12–18.
[19] P.S. Ward, J.R. Cross, C. Lu, O. Weigert, O. Abel-Wahab, R.L. Levine, D.M. Weinstock, K.A. Sharp, C.B. Thompson, Identification of additional idh mutations associated with oncometabolite 2-hydroxyglutarate production, Oncogene 31 (2012) 2491–2498.
[20] B. Björkblom, C. Wibom, M. Eriksson, A.T. Bergenheim, R.L. Sjöberg, P. Jonsson, T. Brännström, H. Antti, M. Sandström, B. Melin, Distinct metabolic hallmarks of who classified adult glioma subtypes, Neuro Oncol. 24 (2022) 1454–1468.
[21] Z.J. Reitman, G. Jin, E.D. Karoly, I. Spasojevic, J. Yang, K.W. Kinzler, Y. He, D.D. Bigner, B. Vogelstein, H. Yan, Profiling the effects of isocitrate dehydrogenase 1 and 2 mutations on the cellular metabolome, Proc. Natl. Acad. Sci. U. S. A. 108 (2011) 3270–3275.
[22] S. Firdous, R. Abid, Z. Nawaz, F. Bukhari, A. Anwer, L.L. Cheng, S. Sadaf, Dysregulated alanine as a potential predictive marker of glioma—an insight from untargeted hrmas-nmr and machine learning data, Metabolites 11 (2021) 507.
[23] S. Tardito, A. Oudin, S.U. Ahmed, F. Fack, O. Keunen, L. Zheng, H. Miletic, P.Ø. Sakariassen, A. Weinstock, A. Wagner, Glutamine synthetase activity fuels nucleotide biosynthesis and supports growth of glutamine-restricted glioblastoma, Nat. Cell Biol. 17 (2015) 1556–1568.
[24] A.J. Wright, G.A. Fellows, J.R. Griffiths, M. Wilson, B.A. Bell, F.A. Howe, *Ex vivo* hrmas of adult brain tumours: metabolite quantification and assignment of tumour biomarkers, Mol. Cancer 9 (2010) 66.
[25] M. Roslin, R. Henriksson, P. Bergström, U. Ungerstedt, A. Tommy Bergenheim, Baseline levels of glucose metabolites, glutamate and glycerol in malignant glioma assessed by stereotactic microdialysis, J. Neuro Oncol. 61 (2003) 151–160.
[26] J.M. Kampa, U. Kellner, C. Marsching, C. Ramallo Guevara, U.J. Knappe, M. Sahin, M. Giampà, K. Niehaus, H. Bednarz, Glioblastoma multiforme: metabolic differences to peritumoral tissue and IDH-mutated gliomas revealed by mass spectrometry imaging, Neuropathology 40 (2020) 546–558.

[27] A. Prabhu, B. Sarcar, S. Kahali, Z. Yuan, J.J. Johnson, K.-P. Adam, E. Kensicki, P. Chinnaiyan, Cysteine catabolism: a novel metabolic pathway contributing to glioblastoma growth, Cancer Res. 74 (2014) 787–796.
[28] R. Simpson, G.A. Devenyi, P. Jezzard, T.J. Hennessy, J. Near, Advanced processing and simulation of MRS data using the fid appliance (FID-A)—an open source, matlab-based toolkit, Magn. Reson. Med. 77 (2017) 23–33.
[29] S.W. Provencher, Automatic quantitation of localized *in vivo* ^{1}H spectra with LCModel, NMR Biomed. 14 (2001) 260–264.
[30] C. Cadrien, S. Sharma, P. Lazen, R. Licandro, J. Furtner, A. Lipka, E. Niess, L. Hingerl, S. Motyka, S. Gruber, 7T magnetic resonance spectroscopic imaging predicting IDH status and glioma grading, Cancer Imaging 24 (2024) 67.
[31] S. Wold, A. Ruhe, H. Wold, I. Dunn, J. William, The collinearity problem in linear regression. The partial least squares (PLS) approach to generalized inverses, SIAM J. Sci. Stat. Comput. 5 (1984) 735–743.
[32] T. Fawcett, An introduction to ROC analysis, Pattern Recognit. Lett. 27 (2006) 861–874.
[33] A. Jiménez-Valverde, Insights into the area under the receiver operating characteristic curve (auc) as a discrimination measure in species distribution modelling, Global Ecol. Biogeogr. 21 (2012) 498–507.
[34] C.M. Andersen, R. Bro, Variable selection in regression—a tutorial, J. Chemometr. 24 (2010) 728–737.
[35] R. Li, W. Zhong, L. Zhu, Feature screening via distance correlation learning, J. Am. Stat. Assoc. 107 (2012) 1129–1139.
[36] P.C. Austin, F.E. Harrell Jr., D. van Klaveren, Graphical calibration curves and the integrated calibration index (ICI) for survival models, Stat. Med. 39 (2020) 2714–2742.
[37] W.S. Cleveland, Robust locally weighted regression and smoothing scatterplots, J. Am. Stat. Assoc. 74 (1979) 829–836.
[38] K. Rufibach, Use of brier score to assess binary predictions, J. Clin. Epidemiol. 63 (2010) 938–939.
[39] D.N. Louis, A. Perry, G. Reifenberger, A. von Deimling, D. Figarella-Branger, W.K. Cavenee, H. Ohgaki, O.D. Wiestler, P. Kleihues, D.W. Ellison, The 2016 world health organization classification of tumors of the central nervous system: a summary, Acta Neuropathol. 131 (2016) 803–820.
[40] G. Hangel, P. Lazen, C. Cadrien, S. Chambers, J. Furtner, L. Hingerl, B. Strasser, B. Kiesel, M. Mischkulnig, M. Preusser, High-resolution mapping of tumor and peritumoral glutamate and glutamine in gliomas using 7T MRSI, Radiol. Imaging Cancer 7 (2025) e240494.
[41] Y. Li, R. Guo, Y. Zhao, W. Jin, Z. Ke, L. Chen, X. Chen, W. Tang, Y. Li, Z.-P. Liang, Multiplexed magnetic resonance imaging, Nature (2026), https://doi.org/10.1038/s41586-026-10475-x.
[42] X. Chen, J. Li, D. Chen, Y. Zhou, Z. Tu, M. Lin, T. Kang, J. Lin, T. Gong, L. Zhu, Cloudbrain-MRS: an intelligent cloud computing platform for *in vivo* magnetic resonance spectroscopy preprocessing, quantification, and analysis, J. Magn. Reson. 358 (2024) 107601.
[43] Z. Tu, J. Zhang, Y. Yang, D. Guo, X. Qu, Dmnet: a reliable magnetic resonance spectroscopy quantification network and the verification on 5T scanners, in: International Society for Magnetic Resonance in Medicine 33rd Scientific Meeting-Ismrm'25, Honolulu, Hawaii, USA, 2025, p. 5151.
[44] Q. Yang, Z. Wang, K. Guo, C. Cai, X. Qu, Physics-driven synthetic data learning for biomedical magnetic resonance: the imaging physics-based data synthesis paradigm for artificial intelligence, IEEE Signal Process. Mag. 40 (2023) 129–140.
[45] Z. Tu, J. Zhang, Y.-H. Chu, L. Lin, X. Jiang, J. Wang, Q. Xu, D. Guo, X. Qu, Multi-vendor physical intelligent network for accurate quantification of magnetic resonance spectroscopy metabolites, in: International Society for Magnetic Resonance in Medicine 33rd Scientific Meeting-ISMRM' 25, Honolulu, Hawaii, USA, 2025, p. 4016.

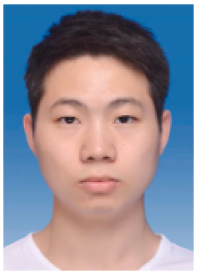

Zhangren Tu received the B.S. degree in communication engineering from East China University of Technology, Nanchang, China, in 2018, and the M.S. degree in optoelectronics and communication engineering from Xiamen University of Technology, Xiamen, China, in 2021. He is currently pursuing the Ph.D. degree with the Department of Electronic Science, Xiamen University, Xiamen, China. His research interests encompass quantitative MRS, clinical applications of MRS, accelerated magnetic resonance spectroscopy and imaging, and deep learning methodologies.

Wanjun Hu is with the Department of Magnetic Resonance Imaging, Lanzhou University Second Hospital, Lanzhou, China. His research focuses on oncologic imaging, particularly the magnetic resonance imaging evaluation of gliomas. His research interests also include the application of artificial intelligence in medical image analysis, tumor characterization, differential diagnosis, treatment response assessment, and prognosis prediction. He is committed to integrating advanced imaging techniques with artificial intelligence to support precise diagnosis and individualized management of patients with brain tumors.

Jialve Zhang received the B.S. degree in Electromagnetic Field and Wireless Technology from Xiamen University, China, in 2022, and the M.S. degree in Electronic Information Engineering from City University of Hong Kong, China, in 2023. He is currently pursuing the Ph.D. degree in Intelligent Instrument and Equipment at Xiamen University, China. His research interests include quantitative magnetic resonance spectroscopy, machine learning, statistical analysis, and their applications in biomedical engineering.

Dairong Cao is a second-grade chief physician (professor-level senior radiologist), doctoral supervisor, and currently Administrative Director of the Department of Medical Imaging at The First Affiliated Hospital of Fujian Medical University, as well as Head/Dean of the Department of Medical Imaging at Fujian Medical University School of Medical Imaging, Fuzhou, China. He serves on the Standing Committees of the Radiology Branch of the Chinese Medical Association and the Chinese Medical Doctor Association, and is an Editorial Board Member of the Chinese Journal of Radiology. His clinical and research expertise focuses on CT and MRI diagnostic imaging of the nervous system, supporting precise diagnosis, treatment planning, and individualized patient management.

Jing Zhang is with the Department of Magnetic Resonance Imaging, Lanzhou University Second Hospital, Lanzhou, China. She has been engaged in clinical imaging diagnosis and research in the field of neurological diseases. Her research interests focus on central nervous system imaging, with particular emphasis on the imaging evaluation of brain tumors and pediatric neurological disorders. She is dedicated to the application of magnetic resonance imaging techniques in disease detection, differential diagnosis, treatment assessment, and prognosis evaluation, aiming to improve the precision of clinical diagnosis and individualized patient management.

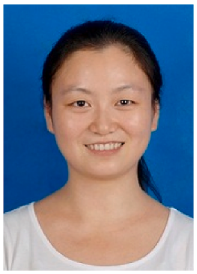

Di Guo received the B.S. and Ph. D. degrees in Communication Engineering from Xiamen University, China, in 2005 and 2012 respectively. She is a Professor with Department of Computer Science and Technology at Xiamen University of Technology, China. From 2018 to 2019, she worked as a visiting scholar in Department of Electrical Engineering at University of Washington, Seattle, USA. She is IEEE Senior Member, and awarded as Fujian Province High level Talent. She won three grants from the National Natural Science Foundation of China. Her research interests include magnetic resonance spectroscopy, artificial intelligence, cloud computing, and their applications in biomedical engineering.

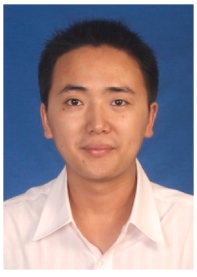

Xiaobo Qu received the B.S. and Ph.D. degrees in communication engineering from Xiamen University, Xiamen, China, in 2006 and 2011, respectively. From 2012 to 2019, he was the Visiting Professor with the University of Gothenburg, Gothenburg, Sweden, The Hong Kong University of Science and Technology, Hong Kong, and the University of Washington, Seattle, WA, USA. He is currently a Professor and Director of Xiamen University-Neusoft Medical Magnetic Resonance Imaging Joint Research and Development Center, the Vice Director of Fujian Provincial Key Laboratory of Plasma and Magnetic Resonance, Xiamen University. His research interests include magnetic resonance imaging and spectroscopy, signal and image representations, computational imaging, machine learning, artificial intelligence, and cloud computing. Dr. Qu has been a senior member of IEEE EMBS and SPS and a member of ISMRM. He was a recipient of the Excellent Young Scientists Fund Award from the National Natural Science Foundation of China in 2021, the First Prize in Natural Science Award of Fujian Province of China in 2022, and the Second Prize of National Teaching Achievement Award in 2023. He is an Associate Editor of IEEE Transactions on Neural Networks and Learning Systems and a Senior Editor of BMC Medical Imaging, and an editor of Magnetic Resonance Letter.